


## PAPER

[View Article Online](#)  
[View Journal](#) | [View Issue](#)Cite this: *Nanoscale Adv.*, 2024, 6, 934

# Augmented photocatalysis induced by 1T-MoS<sub>2</sub> bridged 2D/2D MgIn<sub>2</sub>S<sub>4</sub>@1T/2H-MoS<sub>2</sub> Z-scheme heterojunction: mechanistic insights into H<sub>2</sub>O<sub>2</sub> and H<sub>2</sub> evolution†

Sarmistha Das, Lopamudra Acharya, Lijarani Biswal and Kulamani Parida \*

In the realm of composite photocatalysts, the fusion of the co-catalyst effect with interfacial engineering is recognized as a potent strategy for facilitating the segregation and migration of photo-induced charge carriers. Herein, an innovative mediator-based Z-scheme hybrid, *i.e.* MIS@1T/2H-MoS<sub>2</sub>, has been well designed by pairing MIS with 1T/2H-MoS<sub>2</sub> via a facile hydrothermal strategy as a competent photocatalyst for H<sub>2</sub>O<sub>2</sub> and H<sub>2</sub> generation. The co-catalyst, *i.e.* metallic 1T-phase bridging between semiconducting 2H-MoS<sub>2</sub> and MIS, serves as a solid state electron mediator in the heterostructure. Morphological findings revealed the growth of 1T/2H-MoS<sub>2</sub> nanoflowers over MIS microflowers, verifying the close interaction between MIS and 1T/2H-MoS<sub>2</sub>. By virtue of accelerated e<sup>-</sup>/h<sup>+</sup> pair separation and migration efficiency along with a proliferated density of active sites, the MMS<sub>2</sub>-30 photocatalyst yields an optimum H<sub>2</sub>O<sub>2</sub> of 35 μmol h<sup>-1</sup> and H<sub>2</sub> of 370 μmol h<sup>-1</sup> (ACE of 5.9%), which is 3 and 2.7 fold higher than pristine MIS. This obvious enhancement can be attributed to photoluminescence and electrochemical aspects that substantiate the diminished charge transfer resistance along with improved charge carrier separation, representing a good example of a noble metal-free photocatalyst. The proposed Z-scheme charge transfer mechanism is aided by time-resolved photoluminescence (TRPL), XPS, radical trapping experiments, and EPR analysis. Overall, this endeavour provides advanced insights into the architecture of noble metal-free Z-scheme heterostructures, offering promising prospects in photocatalytic applications.

Received 22nd October 2023  
Accepted 24th December 2023

DOI: 10.1039/d3na00912b

[rsc.li/nanoscale-advances](https://rsc.li/nanoscale-advances)

## Introduction

The significant expansion of industrialization in the current world is giving rise to the two most pressing global issues: energy crisis and environmental pollution.<sup>1,2</sup> Consequently, research communities are actively seeking a long term and unchanging resolution to achieve an eco-friendly society devoid

of pollution, all while reducing our reliance on non-renewable energy resources.<sup>3</sup> Hydrogen peroxide (H<sub>2</sub>O<sub>2</sub>), recognized as an environmental friendly oxidant, has garnered significant interest among the leading researchers owing to its use in various domains, including bleaching, medical sterilization, food and paper making, waste water disinfection and chemical processing, with approximately 2.2 million tons of annual demand.<sup>4,5</sup> H<sub>2</sub>O<sub>2</sub> has also attracted considerable attention as a novel energy carrier for fuel cells as it is water soluble and favourable to be implemented in a single-compartment cell for generating electricity.<sup>6,7</sup> Several techniques involving alcohol oxidation, anthraquinone process, electrochemical synthesis, direct fabrication from hydrogen and oxygen gas mixtures have been developed for H<sub>2</sub>O<sub>2</sub> production.<sup>8–11</sup> Nonetheless, certain drawbacks associated with the above outlined synthesis methods prompts the need for substantial energy input, elevated hazard of explosion from combination of H<sub>2</sub>/O<sub>2</sub> gases, and extensive solvent use.<sup>12</sup> At present, the industrial production of H<sub>2</sub>O<sub>2</sub> relies on the anthraquinone method, consisting of two successive high-energy oxidation and hydrogenation steps considering catalysts based on noble metals, which is both an energy intensive and non-eco-friendly process.<sup>8,13</sup> Therefore, the

Centre for Nano Science and Nano Technology, Institute of Technical Education and Research, Siksha 'O' Anusandhan University, Bhubaneswar-751030, India. E-mail: [kulamaniparida@soa.ac.in](mailto:kulamaniparida@soa.ac.in); [paridakulamani@yahoo.com](mailto:paridakulamani@yahoo.com); Fax: +91-674-2350642; Tel: +91-674-2351777

† Electronic supplementary information (ESI) available: Characterization techniques; photo-electrochemical measurements; photocatalytic H<sub>2</sub>O<sub>2</sub> production experiment; photocatalytic H<sub>2</sub> evolution experiment; Fig. S1. (a) XRD pattern of neat 1T/2H-MoS<sub>2</sub> and (b) FESEM image of MIS microflower. Fig. S2. (a) EDX spectra of MMS<sub>2</sub>-30 composite and (b) elemental mapping of Mg, In, Mo, and S elements for MMS<sub>2</sub>-30. Fig. S3. XPS survey spectra of MMS<sub>2</sub>-30 photocatalyst. Fig. S4. TRPL plot for neat MIS and MMS<sub>2</sub>-30 composite. Fig. S5. XRD pattern for fresh and used MMS<sub>2</sub>-30 photocatalyst. Fig. S6. (a) Scavenger test for MMS<sub>2</sub>-30 towards photocatalytic H<sub>2</sub>O<sub>2</sub> evolution. (b) NBT experiment for 'O<sub>2</sub><sup>-</sup> and (c) EPR spectra for 'O<sub>2</sub><sup>-</sup> in dark and light conditions. Table S1. Comparative study of photocatalytic H<sub>2</sub> evolution. Table S2. Comparative study of photocatalytic H<sub>2</sub>O<sub>2</sub> production. See DOI: <https://doi.org/10.1039/d3na00912b>

need of embracing a green and ecologically sustainable approach is highly on demand.<sup>14–16</sup> Due to remarkable attributes of minimal energy expenditure, enhanced safety measures, and negligible pollution, production of  $\text{H}_2\text{O}_2$  from oxygen and water using photocatalysts *via* artificial photosynthetic process has currently been perceived.<sup>17–19</sup> Furthermore, hydrogen ( $\text{H}_2$ ) holding is promising as a viable eco-friendly alternative to the diminishing non-renewable energy sources and serves as a green, clean and sustainable energy source.<sup>20–22</sup> Researchers are drawn to the intriguing potential of photocatalytic  $\text{H}_2$  generation using semiconductors *via* water splitting owing to its simple process and economic feasibility.<sup>23–25</sup> Several semiconductor oriented materials have been optimized for enhanced photocatalytic generation of  $\text{H}_2\text{O}_2$  as well as  $\text{H}_2$ .

In this regard, attention has been directed towards 2D-transition metal dichalcogenides (TMD) and ternary metal chalcogenides such as thiospinel-type materials. Recently, 2D molybdenum disulphide ( $\text{MoS}_2$ ), *i.e.*, a member of the TMD family, has emerged as a cost-effective and readily available substitute to Pt-based materials owing to its abundant active sites, excellent optoelectronic and structural features along with narrow band gap.<sup>26,27</sup>  $\text{MoS}_2$  exhibits a distinct tri-layered structure in a unique S-Mo-S pattern, where one Mo layer is stacked between two S layers, featuring unsaturated S-atoms at its exposed edges as reactive sites.<sup>26,28</sup> Typically, two primary phases of  $\text{MoS}_2$  are explored in depth: the octahedral metastable metallic 1T-phase and the stable trigonal prismatic semiconducting 2H-phase. Regardless of their respective interesting benefits, phase engineering has lately been focussed on where the 1T-phase is incorporated into the 2H-phase (*i.e.*, 1T/2H- $\text{MoS}_2$ ) for high-end photocatalytic results.<sup>28,29</sup> Integrating 1T- $\text{MoS}_2$  into the 2H-phase exponentially augments electronic conductivity by  $10^7$  times, thus significantly bolstering charge transfer dynamics and reducing electrical transport loss. The developed 1T/2H- $\text{MoS}_2$  nanostructure boasts a high density of active sites on both the basal planes and edges suitable for effective photocatalytic performance.<sup>30,31</sup> The semiconducting 2H- $\text{MoS}_2$  facilitates photon adsorption and the 1T- $\text{MoS}_2$  functions as an  $\text{e}^-$  reservoir. Moreover, the construction of 2D–2D semiconductors having noble metal-free co-catalyst profoundly enhances the photocatalytic behaviour due to stronger interfacial interaction between two semiconductors, good catalytic dispersion, and effective segregation of photo-generated exciton pairs.<sup>32,33</sup> Hence, the establishment of a system with a semiconductor having a band structure compatible with 1T/2H- $\text{MoS}_2$  is demanding as it enhances light absorption and charge carrier transfer efficiency.

Magnesium indium sulphide ( $\text{MgIn}_2\text{S}_4$ ), a ternary metal sulphide resembling that of spinel, features Mg and In at the core of tetrahedron and octahedron, respectively.  $\text{MgIn}_2\text{S}_4$ , owing to its exceptional features, including narrow band gap, good optoelectronic property, and remarkable chemical stability, has achieved wide utility in fields like photoreduction of heavy metal ions, water splitting ( $\text{H}_2$  evolution), environmental pollutant removal, and more.<sup>34,35</sup> However, in comparison to other efficient photocatalysts, the photocatalytic efficacy of ternary metal chalcogenide is somewhat constrained on account of photo-corrosion, weak  $\text{e}^-/\text{h}^+$  pair separation

efficiency, and poor cycle stability test.<sup>34,36</sup> To address these flaws, designing hybrid semiconductors has emerged as a productive approach. Moreover, from a pragmatic perspective, an integrated heterostructure, including two discrete semiconductors closely interlocked through charge transfer, is deemed more favourable. In contrast to the classic type-II heterojunctions, bio-inspired Z-scheme heterojunctions not only enhance light harvesting features and the spatial dispersion of charge carriers but also maintain the elevated redox potentials of photo-induced  $\text{h}^+$  and  $\text{e}^-$ , which is crucial for  $\text{H}_2\text{O}_2$  generation.<sup>32,37</sup> In this context, 1T/2H- $\text{MoS}_2$ @BCN synthesized *via* hydrothermal strategy was applied towards TCH degradation and  $\text{H}_2$  evolution ( $290 \mu\text{mol h}^{-1}$ ) in our previously reported work. Although it gives fascinating results,  $\text{MgIn}_2\text{S}_4$ @1T/2H- $\text{MoS}_2$  is designed to further promote the photocatalytic activity of 1T/2H- $\text{MoS}_2$ .

In light of the above view, using an *in situ* hydrothermal method, we have made an attempt to design a series of mediator-based Z-scheme photocatalysts (*i.e.*,  $\text{MMoS}_2$ - $x$ ,  $x$  = wt% of 1T/2H- $\text{MoS}_2$ ) by combining 1T/2H- $\text{MoS}_2$  nanoflowers with  $\text{MgIn}_2\text{S}_4$  microflowers. The coupling effect among individual materials is verified by subjecting the system to visible light irradiation and assessing its performance towards photocatalytic  $\text{H}_2\text{O}_2$  and  $\text{H}_2$  production. Effective segregation of  $\text{e}^-/\text{h}^+$  pairs, close interfacial interaction, and a broader range of visible light absorption influence the improved photocatalytic behaviour of this novel heterostructure. Also, the involvement of 1T-phase, a cost-effective and abundantly found noble metal-free co-catalyst, reduces the recombination efficiency of the exciton pairs. The growth of 1T/2H- $\text{MoS}_2$  nanoflowers over  $\text{MgIn}_2\text{S}_4$  microflowers results in elevated density of active sites, leading to impressive photocatalytic activity. The current study provides clear guidance regarding the construction and mechanism of the  $\text{MMoS}_2$ -30 composite towards accelerated photocatalytic activity *via* the Z-scheme charge transfer route.

## Experimental section

### Materials used

All the chemicals utilised in synthesizing 1T/2H- $\text{MoS}_2$ ,  $\text{MgIn}_2\text{S}_4$ , and  $\text{MMoS}_2$ - $x$  composites including ammonium bicarbonate ( $\text{NH}_4\text{HCO}_3$ ), ammonium molybdate ( $(\text{NH}_4)_6\text{Mo}_7\text{O}_{24} \cdot \text{H}_2\text{O}$ ), magnesium nitrate ( $\text{Mg}(\text{NO}_3)_2 \cdot 6\text{H}_2\text{O}$ ), indium nitrate ( $\text{In}(\text{NO}_3)_3 \cdot x\text{H}_2\text{O}$ ), and thioacetamide ( $\text{CH}_3\text{CSNH}_2$ ) were procured from Merck, India. They were all of high purity and analytical grade, requiring no further treatment. Throughout the preparation procedure, ethanol and distilled water were employed as solvents.

### Preparation of MIS microflower

Pristine MIS was prepared *via* a facile hydrothermal strategy. Typically, calculated amounts of  $\text{Mg}(\text{NO}_3)_2 \cdot 6\text{H}_2\text{O}$  and  $\text{In}(\text{NO}_3)_3 \cdot x\text{H}_2\text{O}$ , as Mg and In precursors, were ultrasonically dispersed in 50 mL distilled water for about 30 min at room temperature. Subsequently,  $\text{CH}_3\text{CSNH}_2$  was gradually added to the aforementioned solution in a ratio of 1 : 2 : 8 (Mg : In : S) and was ultra-sonicated for 30 min, followed by continuous stirring



at room temperature for an additional 30 min. Thereafter, the homogenous suspension was transferred into a Teflon-lined vessel and was hydrothermally treated at 180 °C for 12 h. The material underwent centrifugation and was rinsed multiple times with ethanol and distilled water, followed by drying at 60 °C in an oven to obtain the product, *i.e.*, Magnesium Indium Sulphide (denoted as MIS).

### Preparation of MIS@1T/2H-MoS<sub>2</sub> composites (MMoS<sub>2</sub>-x)

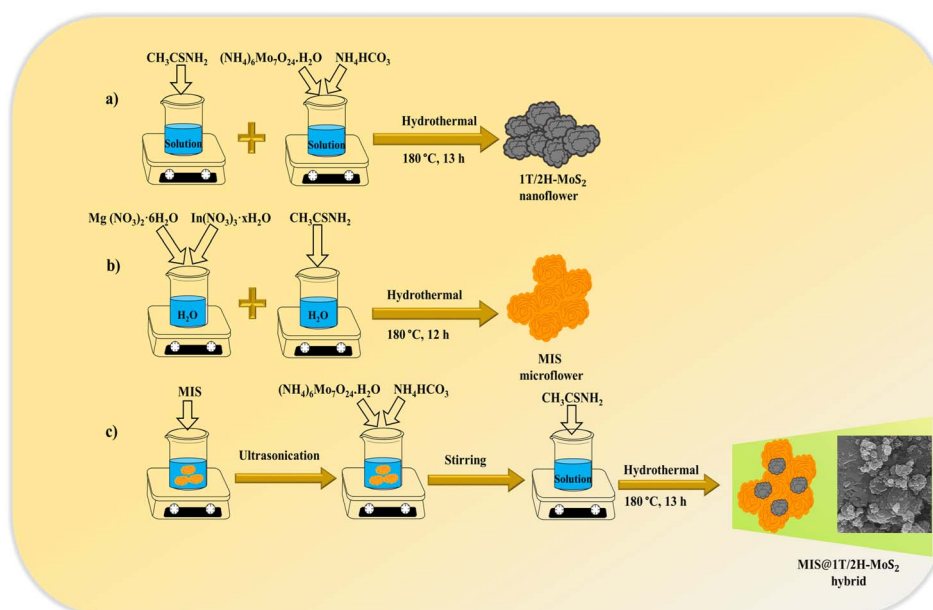
Initially, the synthesized neat MIS (0.3 g) was well-dispersed in 40 mL of distilled water through ultra-sonication for about 1 h, as depicted in Scheme 1. Then, measured quantities of (NH<sub>4</sub>)<sub>6</sub>Mo<sub>7</sub>O<sub>24</sub>·H<sub>2</sub>O and NH<sub>4</sub>HCO<sub>3</sub> were added to the above solution, which underwent 30 min of stirring. Following this, CH<sub>3</sub>CSNH<sub>2</sub> was added to the mixture and stirred for 30 more min at room temperature. The resulting suspension was then transferred into a Teflon-lined vessel for a 13 h hydrothermal treatment at 180 °C. Further, the material was collected by centrifugation followed by several washes with ethanol and distilled water. The final sample obtained after drying at 60 °C in vacuum forms the MIS@1T/2H-MoS<sub>2</sub> composites (referred to as MMoS<sub>2</sub>-x), where x signifies the wt% of 1T/2H-MoS<sub>2</sub> (*i.e.*, 20, 30, 40) with respect to MIS. Likewise, by varying the wt% of 1T/2H-MoS<sub>2</sub> precursors, a set of MIS@1T/2H-MoS<sub>2</sub> photocatalysts were prepared and designated as MMoS<sub>2</sub>-20, MMoS<sub>2</sub>-30 and MMoS<sub>2</sub>-40. Neat 1T/2H-MoS<sub>2</sub> was synthesized by adopting the above identical process without adding MIS.

## Results and discussion

### Structural and morphological analysis

The XRD analysis of the prepared MIS, MMoS<sub>2</sub>-x, and 1T/2H-MoS<sub>2</sub> nanomaterials shown in Fig. 1a and S1a,<sup>†</sup> respectively, are

performed to interpret their phase purity and crystallographic properties. Typically, in Fig. S1a,<sup>†</sup> the two distinct diffraction peaks at 9.2° and 18.4° for (002) and (004) lattice planes, respectively, indicate the presence of the 1T phase in 1T/2H-MoS<sub>2</sub>. The other diffraction peaks at 32.3°, 43.0°, and 57.2° can be attributed to the (100), (103), and (110) planes of 1T/2H-MoS<sub>2</sub>, respectively.<sup>30,38</sup> Concretely, the diffraction patterns for pristine MIS in Fig. 1a display peaks at 14.3°, 23.4°, 27.5°, 28.7°, 33.4°, 43.8°, 48.0°, 56.4°, 59.7°, 67.0°, 70.2° and 77.0° assigned to crystalline planes of (111), (220), (311), (222), (400), (511), (440), (533), (444), (731), (800) and (751), respectively, in reference with JCPDS: 01-070-2893.<sup>35</sup> The XRD patterns of MMoS<sub>2</sub>-x heterojunctions in Fig. 1a closely resembled those of pristine MIS suggesting no significant changes on the crystal planes of MIS by varying the amount of 1T/2H-MoS<sub>2</sub>. Furthermore, as the loading quantity of 1T/2H-MoS<sub>2</sub> increases, the peak intensity of MIS in MMoS<sub>2</sub>-x composites gradually decreases and broadens.<sup>39,40</sup> Interestingly, no discernible peak is observed for 1T/2H-MoS<sub>2</sub>, indicating excellent homogeneity as well as favourable interaction between the two neat components. The fabricated photocatalysts exhibited a high level of phase purity since no additional peaks of metal oxides, unreacted reactants, and binary sulphides were observed. The Raman spectra of neat MIS, 1T/2H-MoS<sub>2</sub>, and MMoS<sub>2</sub>-30 are presented in Fig. S1b<sup>†</sup> for further confirmation of the heterostructure formation. According to the previously reported paper,<sup>30</sup> in neat 1T/2H-MoS<sub>2</sub>, two peaks at 281.5 and 376.7 cm<sup>-1</sup> correspond to E<sub>1g</sub> and E<sub>2g</sub> of 2H-MoS<sub>2</sub>, whereas peaks positioned at 148.6, 194.5, 212.6, 236.4, and 335.7 cm<sup>-1</sup> are assigned to the phonon modes of 1T-MoS<sub>2</sub>. Moreover, for pristine MIS, the peaks obtained at 200–400 cm<sup>-1</sup> are attributed to the vibrational modes of In–S (A<sub>1g</sub>) and Mg–S (E<sub>g</sub>). Owing to the small quantity of 1T/2H-MoS<sub>2</sub>, the Raman spectra of MMoS<sub>2</sub>-30 are quite identical to that of neat MIS. The



**Scheme 1** Synthetic routes for (a) 1T/2H-MoS<sub>2</sub>, (b) MIS and (c) MMoS<sub>2</sub>-x composites via hydrothermal method.





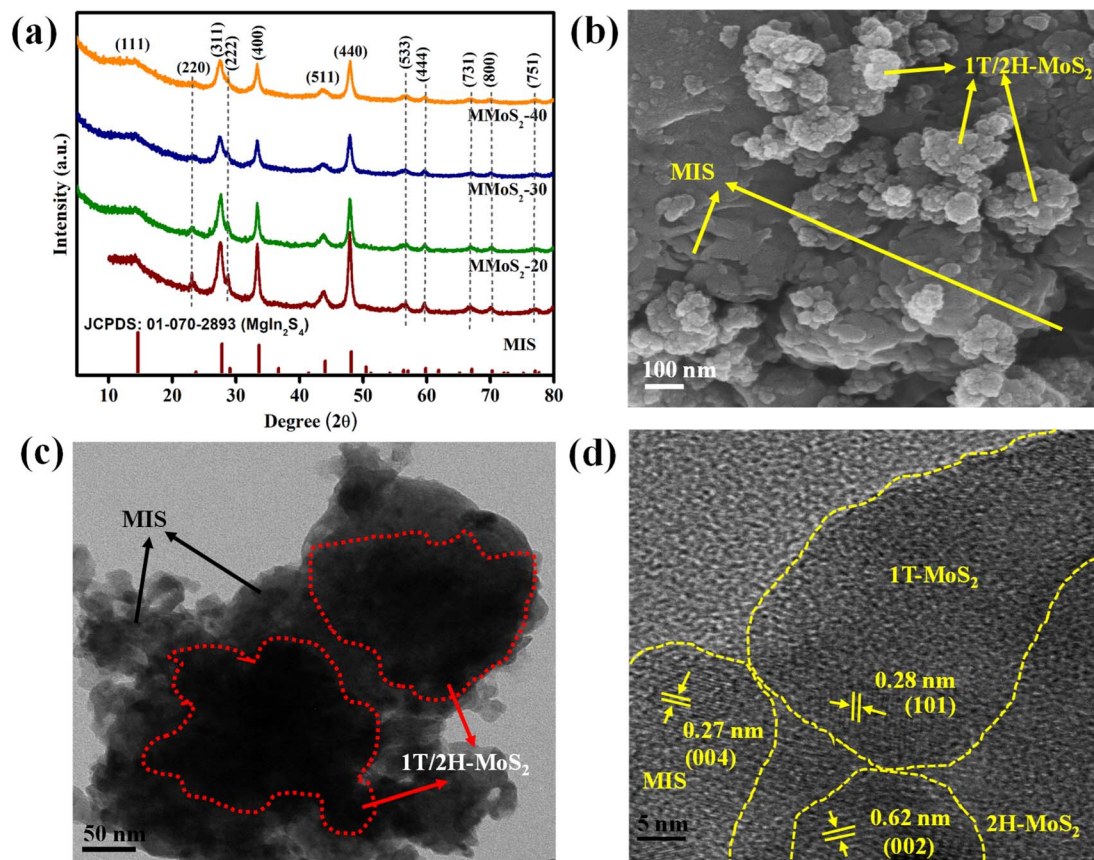


Fig. 1 (a) XRD spectra of neat MIS and prepared MMoS<sub>2</sub>-x photocatalysts. (b) FESEM image and (c and d) HRTEM images of the MMoS<sub>2</sub>-30 composite.

peak intensity of MIS in the MMoS<sub>2</sub>-30 composite is reduced by adding 1T/2H-MoS<sub>2</sub>, revealing the formation of a heterostructure.

Field emission scanning electron microscopy (FESEM) and high-resolution transmission electron microscopy (HRTEM) analyses provide information about the morphological aspects of the synthesized materials, *i.e.*, 1T/2H-MoS<sub>2</sub>, MIS, and their composite MMoS<sub>2</sub>-30. Fig. S1b† displays the FESEM image of pristine MIS showcasing a microflower-like morphology.<sup>35,41</sup> The FESEM image of 1T/2H-MoS<sub>2</sub> reveals the formation of nanoflowers resulting from the entwining of individual edges exposing curved nanopetals as observed from previously reported papers.<sup>32,42</sup> Fig. 1b depicts the FESEM image of MMoS<sub>2</sub>-30 illustrating MIS microflowers surrounded by the arbitrary growth of 1T/2H-MoS<sub>2</sub> nanoflowers that coincides with the HRTEM image in Fig. 1c. As shown in the figure, the MIS microflowers offer a close contact interface with 1T/2H-MoS<sub>2</sub> nanoflowers forming MMoS<sub>2</sub>-30 hybrid. This intensifies the concentration of active sites, contributing towards enhanced photocatalytic activity. In Fig. 1d, two distinct lattice fringes are evident at 0.28 and 0.62 nm, corresponding to the (101) plane of the 1T phase and (002) plane of the 2H phase, respectively, along with a lattice fringe of 0.27 nm for the (004) plane of MIS.<sup>26,31</sup> This indicates the co-existence of neat moieties in the MMoS<sub>2</sub>-30 composite. Moreover, the energy dispersive X-ray

(EDX) spectra for MMoS<sub>2</sub>-30 presented in Fig. S2a† validate the absence of impurities with the existence of all elements (Mo, S, Mg, and In). The consistent distribution of the constituent elements throughout the MMoS<sub>2</sub>-30 hybrid is presented in Fig. S2(b-e),† supplementing additional support for the strong interaction between the pristine materials.

### XPS analysis

X-ray photoelectron spectroscopy (XPS), a surface-specific investigative technique, was employed to assess the existence and valence states of various elements within the prepared photocatalysts. The XPS survey spectra for the MMoS<sub>2</sub>-30 composite in Fig. S3† unequivocally evidence the presence of elements from each parent material, including Mg, In, Mo, and S, which is further substantiated by the findings from EDX and elemental mapping. The Mg 1s core level spectrum in neat MIS showed a single broad peak at 1305.0 eV due to the +2 oxidation state (Fig. 2a). As shown in Fig. 2b, the In 3d XPS spectrum is deconvoluted into doublet peaks around 444.7 and 452.3 eV, corresponding to 3d<sub>5/2</sub> and 3d<sub>3/2</sub>, respectively, of pristine MIS with a peak splitting of 7.68 eV indicating the presence of +3 oxidation state.<sup>35,43</sup> Moreover, in neat 1T/2H-MoS<sub>2</sub>, the deconvoluted Mo 3d peaks for the 1T phase were obtained at 228.5 and 231.7 eV as well as for the 2H phase at 229.3 and 232.6 eV, corresponding to Mo 3d<sub>5/2</sub> and 3d<sub>3/2</sub>, respectively (Fig. 2c).

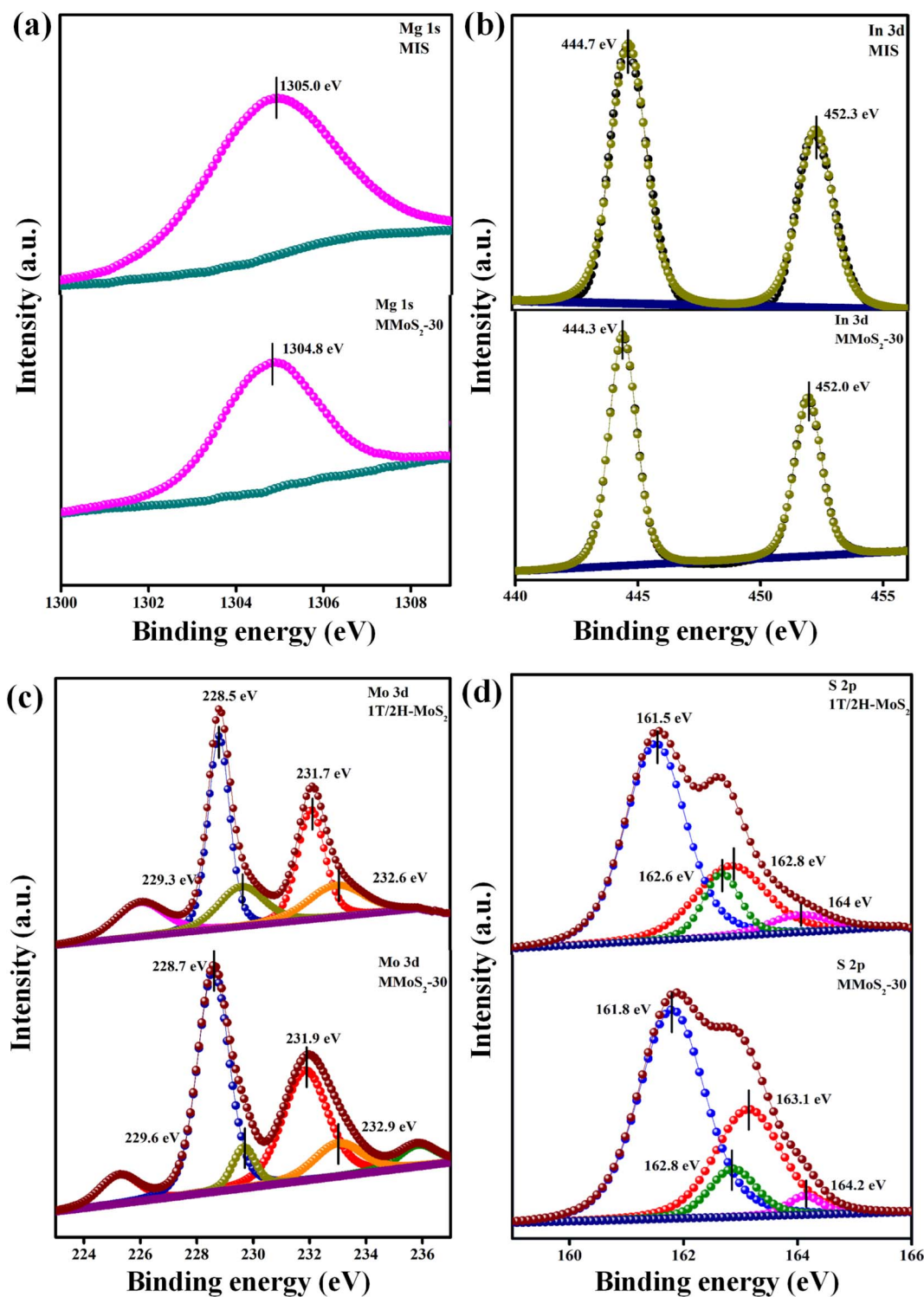


Fig. 2 XPS spectra of neat MIS, 1T/2H-MoS<sub>2</sub> and MMoS<sub>2</sub>-30 composite: (a) Mg 1s, (b) In 3d, (c) Mo 3d, and (d) S 2p.

According to Fig. 2d, four deconvoluted S 2p peaks of neat 1T/2H-MoS<sub>2</sub> were positioned at 161.5 and 162.8 eV for the 1T phase along with binding energies of 162.6 and 164.0 eV for the 2H phase, corresponding to S 2p<sub>3/2</sub> and 2p<sub>1/2</sub> spin states, respectively.<sup>32,41,44</sup> The XPS analysis also yields valuable insights into the electron transfer from 1T/2H-MoS<sub>2</sub> to MIS semiconductor

upon forming a solid state Z-scheme heterostructure. This results in slight positive and negative shifts in the binding energy values of 1T/2H-MoS<sub>2</sub> and MIS in the MMoS<sub>2</sub>-30 composite in contrast to their respective neat counterparts. In comparison to bare MIS, the Mg 1s XPS spectrum in MMoS<sub>2</sub>-30 (Fig. 2a) is shifted to negative binding energy at 1304.8 eV.



Concurrently, the two peaks of In 3d spectra in Fig. 2b are negatively shifted to lower binding energy at 444.3 and 452.0 eV compared to neat MIS. Nevertheless, a positive shift is displayed for the Mo 3d spectrum of MMoS<sub>2</sub>-30 in Fig. 2c, with peaks at 228.7 and 231.9 eV regarding the 1T phase as well as at 229.6 and 232.9 eV for the 2H phase, referring to 3d<sub>5/2</sub> and 3d<sub>3/2</sub>, respectively, than bare 1T/2H-MoS<sub>2</sub>. Simultaneously, S 2p spectra of the MMoS<sub>2</sub>-30 composite also possess a positive shift in binding energies as compared to neat 1T/2H-MoS<sub>2</sub> (Fig. 2d). The 1T phase has peak values situated at 161.8 and 163.1 eV along with 162.8 and 164.2 eV for the 2H phase designated to the respective spin states of S (*i.e.*, S 2p<sub>3/2</sub> and S 2p<sub>1/2</sub>). The findings indicated that the electron density of respective materials in the MMoS<sub>2</sub>-30 heterostructure was altered by virtue of electron transfer from 1T/2H-MoS<sub>2</sub> to MIS *via* 1T-MoS<sub>2</sub> mediator. Overall, the transfer of electrons from 1T/2H-MoS<sub>2</sub> to MIS elevates the density of electrons on the MIS surface, thereby shifting the binding energies to lower values (*i.e.*, red shift). Conversely, in 1T/2H-MoS<sub>2</sub>, the binding energy is shifted to higher values (*i.e.*, blue shift) owing to the reduced electron density on the 1T/2H-MoS<sub>2</sub> surface. Such interaction resulted in an inherent electric field within the system that serves as a driving force enabling the transit of photo-induced e<sup>-</sup>/h<sup>+</sup> pairs on exposure to visible light.

### Optical properties

Considering the significance of light absorption ability in photocatalysis, the optical responses of the prepared neat and composite materials were assessed using UV-vis DRS spectral analysis. According to Fig. 3a, pristine MIS exhibits a distinct absorption threshold in the visible light zone around 635 nm, whereas neat 1T/2H-MoS<sub>2</sub> displays broad absorption spectra from UV to NIR region.<sup>32,45</sup> The gradual rise in the loading content of 1T/2H-MoS<sub>2</sub> in MIS boosts the light-harvesting skill of MMoS<sub>2</sub>-*x* heterostructures accompanied by a red shift towards the visible light region in contrast to bare MIS. This evidences a broader visible light response of the MMoS<sub>2</sub>-*x* hybrid, revealing a firmly established design between two pristine frameworks, which results in an escalated rate of photo-excitation for enhanced photocatalytic behaviour. Moreover, by using the Tauc plot, the band gap energies (*E<sub>g</sub>*) of neat 1T/2H-MoS<sub>2</sub> and MIS are determined from the Schuster Kubelka-Munk eqn (1) and (2), respectively.

$$\alpha h\nu = A(h\nu - E_g)^{n/2} \quad (1)$$

$$\alpha h\nu = A(h\nu - E_g)^n \quad (2)$$

The Planck's constant and the absorption coefficient are referred to as *h* and  $\alpha$ , respectively, with *A* serving as a constant and *n* signifying the electronic transition. *E<sub>g</sub>* and  $\nu$  represent band gap energy and frequency of light, respectively. With the use of eqn (1) and (2), the calculated band gap energies (*E<sub>g</sub>*) of 1T/2H-MoS<sub>2</sub> and MIS are 1.23 and 2.12 eV, respectively, as depicted in Fig. 3b and c.<sup>30,46</sup>

Furthermore, the lifetime of photo-induced e<sup>-</sup>/h<sup>+</sup> pairs is a pre-requisite for improved photocatalytic performance. In this

regard, the photoluminescence analysis of the synthesized photocatalysts is represented in Fig. 3d, which provides valuable insights regarding their intricate properties, such as the segregation and recombination efficiency of photo-generated charge carriers. In pristine MIS, an emission peak around 550 nm is observed in contrast to other MMoS<sub>2</sub>-*x* composites. Furthermore, the inclusion of 1T/2H-MoS<sub>2</sub> into MIS resulted in a significant decrease in the emission peak. With the progressive rise in 1T/2H-MoS<sub>2</sub> loading, the PL peak intensity of MMoS<sub>2</sub>-*x* photocatalysts shrinks. Among all, the MMoS<sub>2</sub>-30 composite displayed a reduced PL peak intensity, highlighting enhanced charge carrier segregation and migration with a lower rate of recombination.<sup>35</sup> This can be attributed to the effective coupling between both the neat materials (*i.e.*, 1T/2H-MoS<sub>2</sub> and MIS), resulting in augmented photocatalytic performance. Additionally, time-resolved photoluminescence (TRPL) analysis is conducted for MIS and MMoS<sub>2</sub>-30 photocatalyst to study the average lifespan of the excitons. The decay curves were fitted using a bi-exponential function as given in eqn (3).

$$\text{Fit} = A + \alpha_1 \exp\{-t/\tau_1\} + \alpha_2 \exp\{-t/\tau_2\} \quad (3)$$

$\alpha_1$  and  $\alpha_2$  refer to relative contributions,  $\tau_1$  and  $\tau_2$  denote the decay lifetimes of the respective materials, and *A* is a constant. The average lifespan ( $\tau_{\text{avg}}$ ) of neat MIS and MMoS<sub>2</sub>-30 composite is computed using eqn (4).

$$\tau_{\text{avg}} = \frac{\alpha_1 \tau_1^2 + \alpha_2 \tau_2^2}{\alpha_1 \tau_1 + \alpha_2 \tau_2} \quad (4)$$

The MMoS<sub>2</sub>-30 hybrid exhibited a shorter average lifetime of 0.61 ns in comparison to neat MIS with an average lifetime of 0.86 ns, as depicted in Fig. S4.† This variation in  $\tau_{\text{avg}}$  can be ascribed to the Z-scheme charge dynamics of the heterostructure.<sup>24,32,47</sup>

### Electrochemical properties

The EIS analysis is performed to further explore the effective separation efficiency as well as the rapid transfer of exciton pairs (e<sup>-</sup>/h<sup>+</sup>) in the prepared photocatalysts. The Nyquist plot shows a high-frequency region represented by a semicircle and a low-frequency region denoted by a straight line. Fig. 4a displays the Nyquist plots for 1T/2H-MoS<sub>2</sub>, MIS, and MMoS<sub>2</sub>-30 photocatalysts. As shown in Fig. 4a, the MMoS<sub>2</sub>-30 photocatalyst exhibits a relatively smaller semicircular arc with respect to its parent materials, which implies a declined charge transfer resistance, ultimately leading to improved electrical conductivity of the composite. Also, the EIS observation of the MMoS<sub>2</sub>-30 heterostructure strongly supports the photoluminescence (PL) outcome. Hence, the MMoS<sub>2</sub>-30 composite with respect to its parent materials exhibited higher separation and lower rate of e<sup>-</sup>/h<sup>+</sup> pair recombination owing to the mediator-based Z-scheme charge transfer dynamics upgrading the photocatalytic activity.<sup>48,49</sup>

Using the Mott-Schottky technique, the nature and flat band potential (*E<sub>fb</sub>*) of the pristine materials can be determined, which is further considered in evaluating the band edge





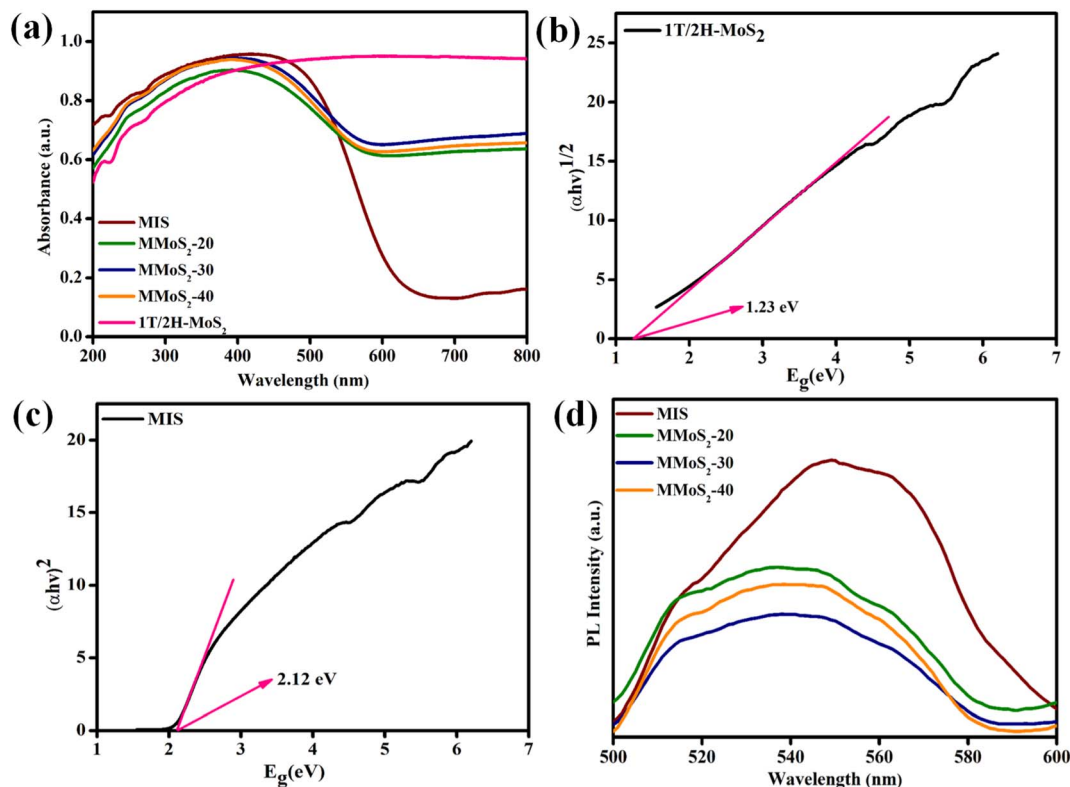


Fig. 3 (a) UV-vis DRS of prepared materials. Band gap energy plots of (b) 1T/2H-MoS<sub>2</sub>, (c) MIS and (d) PL spectra of MIS and MMS<sub>2</sub>-x composites.

potentials of the semiconducting materials. The MS-plot for both the parent semiconductors, *i.e.*, 1T/2H-MoS<sub>2</sub>, MIS, and MMS<sub>2</sub>-30 composite in Fig. 4b–d, shows positive slopes with flat band potentials  $E_{fb}$  such as  $-0.29$ ,  $-1.45$ , and  $-0.21$  V, respectively, revealing themselves to be n-type semiconductors. Subsequently, the conduction band edge potential ( $E_{CB}$ ) of both 1T/2H-MoS<sub>2</sub> and MIS can be evaluated using the following eqn (5),

$$E_{NHE} = E_{Ag/AgCl} + E_{Ag/AgCl} - 0.0591 (7 - \text{pH of the electrolyte}) \quad (5)$$

Using the above equation, the  $E_{CB}$  of 1T/2H-MoS<sub>2</sub> and MIS was calculated to be  $-0.4$  and  $-1.26$  V, respectively. Furthermore, considering the obtained  $E_{CB}$  and  $E_g$ , the respective valence band edge potentials ( $E_{VB}$ ) for 1T/2H-MoS<sub>2</sub> and MIS were determined to be  $0.7$  and  $0.86$  V by implementing eqn (6),

$$E_{VB} = E_g + E_{CB} \quad (6)$$

Moreover, for better insights into the exciton electron-hole separation efficacy, the transient photocurrent analysis is executed for 1T/2H-MoS<sub>2</sub>, MIS, and MMS<sub>2</sub>-30 under a series of alternative dark and visible light irradiating conditions, as shown in Fig. 4e. Under visible light illumination, the materials exhibited a significant rise in photocurrent that remained relatively stable during the light exposure. However, once the light is turned off, a sudden drop in the current density is

observed.<sup>45,50</sup> According to Fig. 4e, the photocurrent densities achieved for neat 1T/2H-MoS<sub>2</sub> and MIS were  $0.45$  and  $0.21 \mu\text{A cm}^{-2}$ , respectively, suggesting the poor charge carrier segregation ability of neat materials. However, due to the mediator-based Z-scheme mechanism, the MMS<sub>2</sub>-30 composite showed a hike in current density around  $1.8 \mu\text{A cm}^{-2}$ , 4 and 8.5 times higher than that of 1T/2H-MoS<sub>2</sub> and MIS, respectively. This affirms the enhanced  $e^-/h^+$  pair separation and migration ability in the MMS<sub>2</sub>-30 heterostructure in contrast to its neat materials.

### Photocatalytic applications

The photocatalytic properties of the as-prepared materials were performed *via* photocatalytic H<sub>2</sub> generation and H<sub>2</sub>O<sub>2</sub> production, and the results are precisely discussed as follows.

#### Photocatalytic H<sub>2</sub> evolution

The hydrogen generation rates of the synthesized photocatalysts are displayed in Fig. 5a. The blank experiment evidenced the pivotal role of photocatalysts as well as light during the photocatalytic hydrogen evolution reaction since the absence of both light and photocatalyst shows no hydrogen gas production.<sup>51–53</sup> A poor hydrogen evolution rate of  $140$  and  $150.3 \mu\text{mol h}^{-1}$  was observed for pristine MIS and 1T/2H MoS<sub>2</sub> due to its quick recombination of charge carriers, as shown in Fig. 5a. Moreover, the loading of 1T/2H MoS<sub>2</sub> to MIS resulted in the augmented hydrogen evolution rate of MMS<sub>2</sub>-x composites



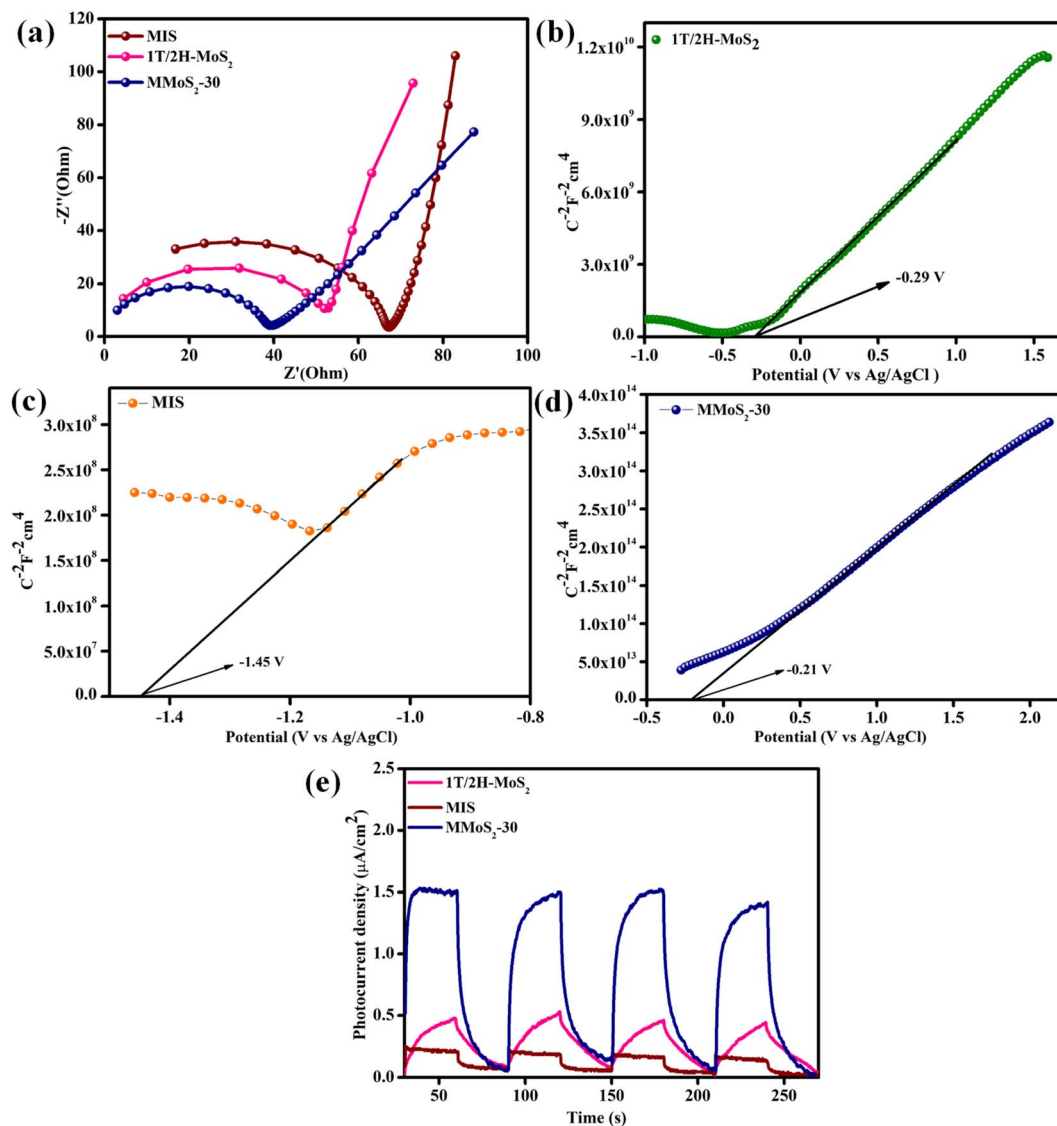


Fig. 4 (a) EIS plot of neat components and the prepared MMoS<sub>2</sub>-30 composite. Mott-Schottky plots of (b) 1T/2H-MoS<sub>2</sub>, (c) MIS and (d) MMoS<sub>2</sub>-30. (e) Transient photocurrent measurement of neat 1T/2H-MoS<sub>2</sub>, MIS, and MMoS<sub>2</sub>-30.

owing to the synergistic effect of heterojunction created between both the individual materials and the increased metallic nature of 1T-MoS<sub>2</sub> providing suitable availability of electrons with densely exposed active sites. The H<sub>2</sub> generation rates for MMoS<sub>2</sub>-20, MMoS<sub>2</sub>-30, and MMoS<sub>2</sub>-40 were obtained to be 321.6, 370, and 298 μmol h<sup>-1</sup>, respectively. As per Fig. 5a, amongst all the synthesized composites, MMoS<sub>2</sub>-30 exhibited the highest H<sub>2</sub> evolution rate, which is 2.7 times that of neat MIS. However, the decreased rate of H<sub>2</sub> evolution by the overloading of 1T/2H-MoS<sub>2</sub> ascribed that the active sites of MIS might get shielded by the black-coloured 1T/2H-MoS<sub>2</sub> obstructing the absorption of photons. Fig. 5b presents the linearly enhanced photocatalytic H<sub>2</sub> evolution of all the materials with increased time, with MMoS<sub>2</sub>-30 having optimum H<sub>2</sub> evolution.

Furthermore, the photostability of MMoS<sub>2</sub>-30 towards photocatalytic H<sub>2</sub> evolution was executed under the same reaction

conditions for consecutive 4 reaction cycles, as displayed in Fig. 5c. The figure depicts no remarkable deviation in activity during the four reaction cycles, which verified the stability of the material for its practical applications. The apparent conversion efficiency (ACE) of MMoS<sub>2</sub>-30 was evaluated to be 5.9 by applying eqn (7),

$$\text{ACE} = \frac{\text{stored chemical energy}}{\text{incident light intensity}} \times 100 \quad (7)$$

### Photocatalytic H<sub>2</sub>O<sub>2</sub> evolution

The photocatalytic H<sub>2</sub>O<sub>2</sub> production by the as-prepared photocatalysts was conducted in oxygen-bubbled water with visible light illumination for 2 h, and the results are presented in Fig. 6a. As shown in the figure, neat MIS and 1T/2H-MoS<sub>2</sub> exhibited poor H<sub>2</sub>O<sub>2</sub> generation rates of 11.84 and 13.6 μmol





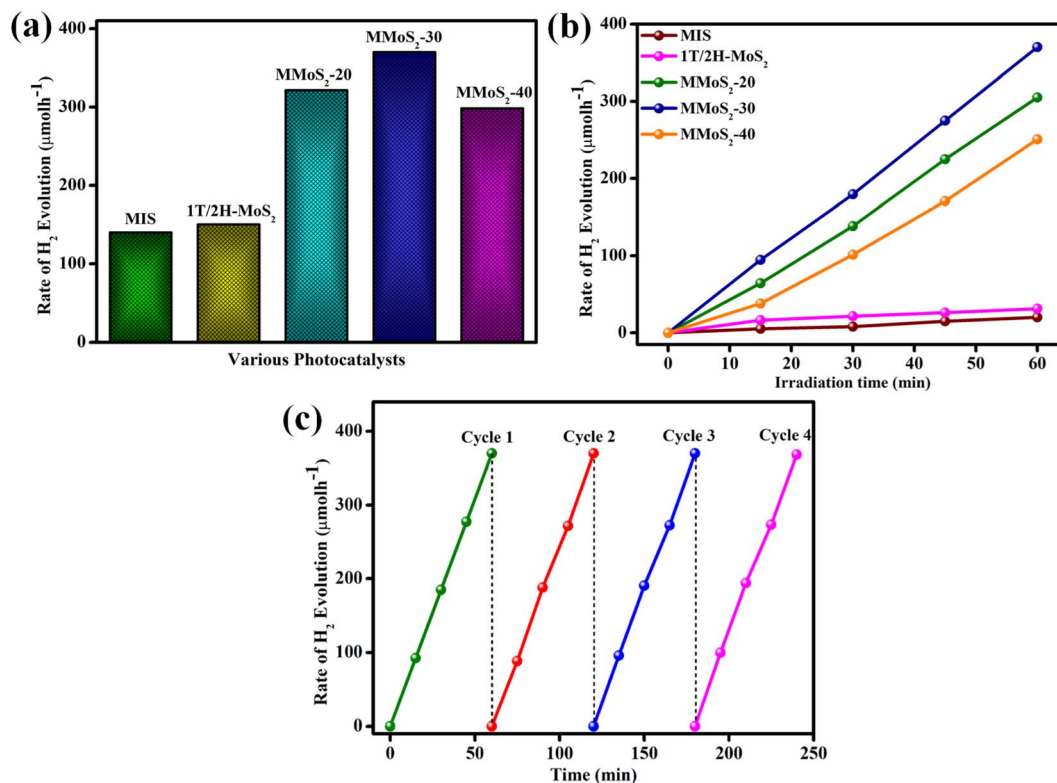


Fig. 5 (a and b) Hydrogen production rate of MIS, 1T/2H-MoS<sub>2</sub>, and synthesized MMoS<sub>2</sub>-*x* photocatalysts and (c) reusability experiment of the MMoS<sub>2</sub>-30 composite.

h<sup>-1</sup> attributing to its quick recombination rate of e<sup>-</sup>/h<sup>+</sup> pairs. The coupling of 1T/2H-MoS<sub>2</sub> nanoflower with MIS microflower remarkably enhanced the photocatalytic H<sub>2</sub>O<sub>2</sub> production of MMoS<sub>2</sub>-*x* composites in the order MMoS<sub>2</sub>-40 < MMoS<sub>2</sub>-20 < MMoS<sub>2</sub>-30 after the formation of the Z-scheme heterojunction between both the neat moieties. MMoS<sub>2</sub>-*x* nanocomposites with increasing content of 1T/2H-MoS<sub>2</sub>, up to 30% with respect to the weight of neat MIS, exhibited increased H<sub>2</sub>O<sub>2</sub> generation rates, *i.e.*, MMoS<sub>2</sub>-20 (29.34 μmol h<sup>-1</sup>) and MMoS<sub>2</sub>-30 (35 μmol h<sup>-1</sup>). However, with further addition of 1T/2H-MoS<sub>2</sub> to 40%, a deviation in the photocatalytic H<sub>2</sub>O<sub>2</sub> production efficiency was noticed at 25.7 μmol h<sup>-1</sup> for MMoS<sub>2</sub>-40, indicating hindrance in the photon energy absorption due to the excess loading of 1T/2H-MoS<sub>2</sub>. The results demonstrated that lower and higher loadings of 1T/2H-MoS<sub>2</sub> were subjected to decreased photocatalytic H<sub>2</sub>O<sub>2</sub> production. Therefore, an appropriate amount of the pristine 1T/2H-MoS<sub>2</sub> is essential for the improved charge carrier migration and separation, thus facilitating the photocatalytic performance of the MMoS<sub>2</sub>-30 heterostructure.

Since the photocatalytic H<sub>2</sub>O<sub>2</sub> production reaction was executed under an oxygen-saturated atmosphere, a comparison study was performed under O<sub>2</sub> and Ar-saturated conditions to examine the impact of oxygen on the H<sub>2</sub>O<sub>2</sub> production rate. As displayed in Fig. 6b, the H<sub>2</sub>O<sub>2</sub> generation rate of MMoS<sub>2</sub>-30 in the presence of Ar-saturated water is significantly lower than that in the oxygen atmosphere, suggesting that the oxygen atmosphere plays a pivotal role in accelerated H<sub>2</sub>O<sub>2</sub> production.<sup>54</sup> Furthermore, the stability of the synthesized material

MMoS<sub>2</sub>-30 was determined by performing the reusability of photocatalytic H<sub>2</sub>O<sub>2</sub> reaction for consecutive 4 cycles up to 480 min. Fig. 6c revealed that the prepared material maintains its stability as the photocatalytic activity shows no significant changes even after 4 successive reaction cycles.

After the assessment of the reusability test, XRD and XPS analyses were performed for the used MMoS<sub>2</sub>-30 sample, as illustrated in Fig. S5,† revealing negligible variation in the stability of the photocatalyst. The superior photocatalytic behaviour of MMoS<sub>2</sub>-30 nanocomposite in terms of H<sub>2</sub> and H<sub>2</sub>O<sub>2</sub> production has been contrasted with those of the alternative semiconductor-based photocatalysts under several parameters, and the outcomes are summarized in Tables S1 and S2,† respectively.

### Mechanistic approach

Based on the aforementioned experimental findings, a possible mechanism for the photocatalytic reaction (H<sub>2</sub> evolution and H<sub>2</sub>O<sub>2</sub> formation) of the as-prepared MMoS<sub>2</sub>-30 photocatalyst is envisioned and illustrated in Scheme 2. The combined result of UV-Vis DRS spectra and Mott-Schottky (MS) analysis reveal the band edge potentials for MIS, *i.e.*  $E_{VB} = 0.86$  and  $E_{CB} = -1.26$  V while for 1T/2H-MoS<sub>2</sub>,  $E_{VB} = 0.7$  and  $E_{CB} = -0.4$  V. Considering the band edge potentials, a bio-inspired solid state Z-scheme mechanism was followed by photo-induced electrons *via* the 1T-phase electron mediator. On exposure to visible light, both the individual materials are capable of developing photo-generated holes and electrons in their respective VB and CB. Propelled by



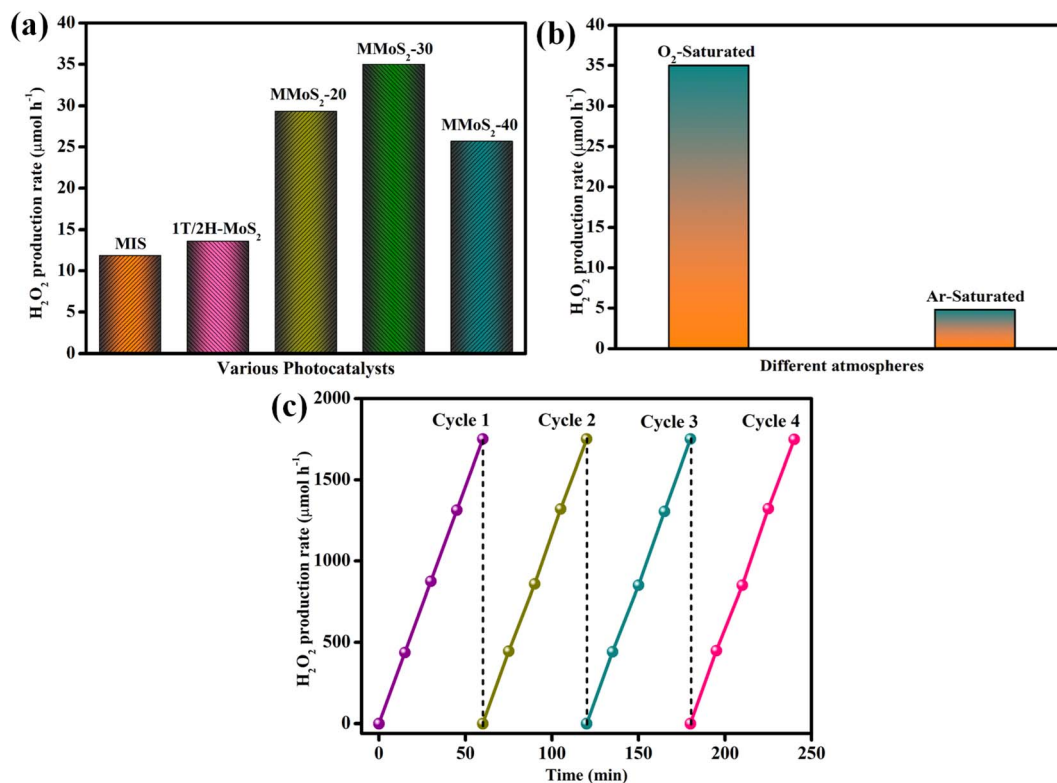
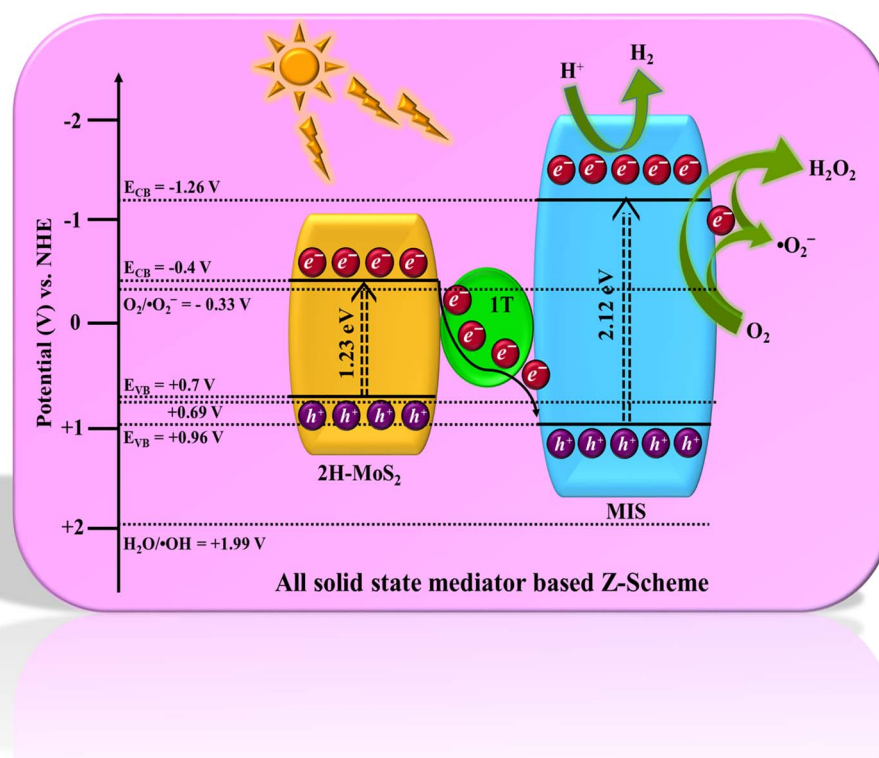


Fig. 6 (a) Rate of photocatalytic H<sub>2</sub>O<sub>2</sub> evolution by neat MIS, 1T/2H-MoS<sub>2</sub> and MMoS<sub>2</sub>-30 photocatalyst. (b) Photocatalytic H<sub>2</sub>O<sub>2</sub> production by MMoS<sub>2</sub>-30 composite under different atmospheres and (c) photostability test of the MMoS<sub>2</sub>-30 photocatalyst for photocatalytic H<sub>2</sub>O<sub>2</sub> evolution.



Scheme 2 Schematic representation of the proposed mediator-based Z-scheme charge transfer mechanism of the MMoS<sub>2</sub>-30 photocatalyst for photocatalytic H<sub>2</sub>O<sub>2</sub> and H<sub>2</sub> production under visible light irradiation.

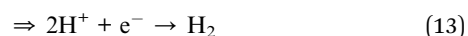
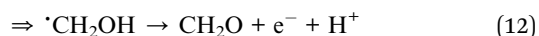
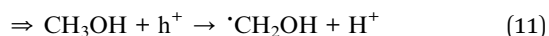
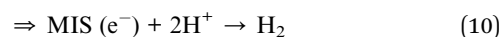
the strong inherent electric field created in the  $\text{MMoS}_2$ -30 photocatalyst, the photo-induced electrons move through metallic 1T- $\text{MoS}_2$ , transitioning from the CB of 2H- $\text{MoS}_2$  to the VB of MIS by merging with the holes within the solid state Z-scheme heterostructure.<sup>32,33</sup> Holes present in the VB of MIS oxidize ethanol to generate protons, increasing electron availability in the CB of MIS. The CB of MIS possesses a potential that is more negative than the redox potential of  $\text{O}_2$ , enabling the production of  $\text{H}_2\text{O}_2$  ( $-0.33$  V for one electron two-step pathway or  $+0.69$  V for two electron single step pathway).<sup>24,45</sup> Consequently, the electrons present on the CB of MIS generate  $\text{H}_2$  from water reduction as the CB of MIS satisfied the potential required ( $\text{H}_2\text{O}/\text{H}_2 = -0.41$  eV) for water reduction as displayed in Scheme 2.<sup>55,56</sup> This process enhances the separation efficiency of exciton pairs, reducing their tendency of rapid recombination that leads to elevated photocatalytic activity. Furthermore, this Z-scheme mediated charge transfer pathway was substantiated by the shifting of binding energies of elements in  $\text{MMoS}_2$ -30 from XPS analysis, as previously discussed. Additionally, scavenger test experiments were performed to clarify the mechanism mentioned above. To study the influence of  $\cdot\text{OH}$ ,  $\text{h}^+$ ,  $\text{e}^-$ , and  $\cdot\text{O}_2^-$  in photocatalytic  $\text{H}_2\text{O}_2$  generation, an array of scavenging agents comprising isopropanol (IPA), citric acid (CA), dimethyl sulfoxide (DMSO), and *para*-benzoquinone (PBQ) were added, respectively. According to Fig. S6a,† with the inclusion of DMSO and PBQ, a noticeable reduction in the efficacy of  $\text{H}_2\text{O}_2$  generation occurred, indicating  $\text{e}^-$  and  $\cdot\text{O}_2^-$  to be the dominant active species towards  $\text{O}_2$  reduction *via* both the two-electron single step and one electron two-step pathway. Conversely, the participation of IPA and CA did not significantly impede the photocatalytic generation of  $\text{H}_2\text{O}_2$ . This implied that  $\cdot\text{OH}$  and  $\text{h}^+$  are not the primary reactive species responsible for  $\text{O}_2$  reduction. Again, to investigate the Z-scheme charge transfer dynamics of  $\text{MMoS}_2$ -30 towards the robust photocatalytic performance, NBT (nitroblue tetrazolium) test was carried out. As shown in Fig. S6b,† a decrease in the peak intensity of  $\text{MMoS}_2$ -30 was observed compared to the pristine MIS, confirming the detection of a higher concentration of  $\cdot\text{O}_2^-$  radicals in the case of  $\text{MMoS}_2$ -30. Further, electron paramagnetic resonance spin trap analysis (EPR) was conducted as a confirmatory test for  $\cdot\text{O}_2^-$  radical formation (Fig. S6c†). The quartet signal with a 1 : 1 : 1 : 1 ratio for  $\text{MMoS}_2$ -30 was obtained in the presence of light, indicating the formation of  $\cdot\text{O}_2^-$  radicals.  $\text{MMoS}_2$ -30 displayed no signal in the dark condition, attributing that in the presence of light, the availability of  $\cdot\text{O}_2^-$  radicals is higher over  $\text{MMoS}_2$ -30 owing to the Z-scheme heterojunction.<sup>57</sup> Hence, the synergistic effect developed between 1T/2H- $\text{MoS}_2$  and MIS leads to the augmented photocatalytic activity for both  $\text{H}_2$  ( $370 \mu\text{mol h}^{-1}$ ) and  $\text{H}_2\text{O}_2$  ( $35 \mu\text{mol h}^{-1}$ ) evolution process, which can be attributed to the following factors:

(i) Development of *in situ* generated 1T/2H- $\text{MoS}_2$  nano-flowers over MIS microflowers offering a multitude of active sites for both  $\text{H}_2\text{O}_2$  and  $\text{H}_2$  generation.<sup>58</sup>

(ii) The metallic 1T-phase in the heterostructure functions exceptionally as an electron reservoir and intermediary between 2H- $\text{MoS}_2$  and MIS.<sup>32</sup>

(iii) Also, the intricate interactions between the neat counterparts, effective separation of exciton pairs with reduced recombination rate, enhanced current density, and lesser charge transfer resistance, as discussed in the PL, TRPL, transient photocurrent, and EIS measurements, boost the photocatalytic performance of the  $\text{MMoS}_2$ -30 composite.

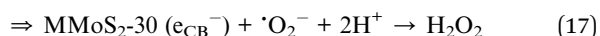
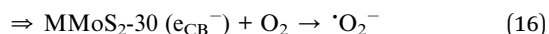
A detailed explanation of the successive steps followed by  $\text{MMoS}_2$ -30 photocatalyst for photocatalytic  $\text{H}_2$  production (eqn (8)–(13)) and  $\text{H}_2\text{O}_2$  generation (eqn (14)–(18)) are given below-equations for  $\text{H}_2$  production



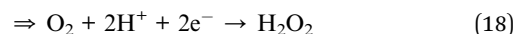
Equations for  $\text{H}_2\text{O}_2$  generation



Single-electron two step



Two-electron single step



## Conclusion

Concisely, MIS@1T/2H- $\text{MoS}_2$  (*i.e.*,  $\text{MMoS}_2$ -*x*) photocatalysts are successfully fabricated *via* a simple hydrothermal strategy without any surfactants where MIS microflowers are embellished with 1T/2H- $\text{MoS}_2$  nanoflowers. In the proposed Z-scheme charge dynamics of the system, the 1T-phase serves as a high flux electron mediator. The designed hybrids were applied as efficient photocatalysts towards  $\text{H}_2\text{O}_2$  generation and  $\text{H}_2$  production on exposure to visible light. Notably, MIS@1T/2H- $\text{MoS}_2$  heterostructure with 30% loading of 1T/2H- $\text{MoS}_2$  (*i.e.*,  $\text{MMoS}_2$ -30) stands out with remarkable improvements in  $\text{H}_2\text{O}_2$  yield reaching  $35 \mu\text{mol h}^{-1}$  and  $\text{H}_2$  evolution rate of  $370 \mu\text{mol h}^{-1}$  being 3 and 2.7 times higher than pristine MIS, respectively. The ameliorated photocatalytic activity characterized by reduced PL peak intensity, decreased arc radius in the Nyquist plot, extended TRPL lifespan, and elevated photocurrent densities can be attributed to the swift charge carrier separation



facilitated by high electron transport *via* 1T-MoS<sub>2</sub> in the Z-scheme charge kinetics. The incorporation of 1T/2H-MoS<sub>2</sub> in small quantities amplifies the absorption capability of MMoS<sub>2</sub>-*x* photocatalysts, significantly contributing to their overall efficiency. Moreover, the promising photostability obtained from reusability tests of the MMoS<sub>2</sub>-30 hybrid validates its feasibility for practical utilization. This study offers a fresh outlook for the design and development of Z-scheme oriented noble metal-free co-catalyst-based heterostructure with appreciable potential for visible light photocatalysis.

## Conflicts of interest

There are no conflicts to declare.

## Acknowledgements

The authors are very much thankful to S'O'A (Deemed to be University) management for their support and encouragement.

## References

- 1 D. Huang, S. Chen, G. Zeng, X. Gong, C. Zhou, M. Cheng, W. Xue, X. Yan and J. Li, *Coord. Chem. Rev.*, 2019, **385**, 44–80.
- 2 C. Gao, J. Low, R. Long, T. Kong, J. Zhu and Y. Xiong, *Chem. Rev.*, 2020, **120**, 12175–12216.
- 3 Y. Qian, F. Zhang and H. Pang, *Adv. Funct. Mater.*, 2021, **31**, 2104231.
- 4 W. Zhao, P. Yan, B. Li, M. Bahri, L. Liu, X. Zhou, R. Clowes, N. D. Browning, Y. Wu, J. W. Ward and A. I. Cooper, *J. Am. Chem. Soc.*, 2022, **144**, 9902–9909.
- 5 S. Yang, A. Verdager-Casadevall, L. Arnarson, L. Silvoli, V. Colic, R. Frydendal, J. Rossmeisl, I. Chorkendorff and I. E. Stephens, *ACS Catal.*, 2018, **8**, 4064–4081.
- 6 H. I. Kim, Y. Choi, S. Hu, W. Choi and J. H. Kim, *Appl. Catal., B*, 2018, **229**, 121–129.
- 7 L. Wang, J. Zhang, Y. Zhang, H. Yu, Y. Qu and J. Yu, *Small*, 2022, **18**, 2104561.
- 8 F. Sandelin, P. Oinas, T. Salmi, J. Paloniemi and H. I. Haario, *Eng. Chem. Res.*, 2006, **45**, 986–992.
- 9 C. M. Crombie, R. J. Lewis, R. L. Taylor, D. J. Morgan, T. E. Davies, A. Folli, D. M. Murphy, J. K. Edwards, J. Qi, H. Jiang and C. J. Kiely, *ACS Catal.*, 2021, **11**, 2701–2714.
- 10 J. K. Edwards, N. E. Ntanjua, A. F. Carley, A. A. Herzing, C. J. Kiely and G. J. Hutchings, *Angew. Chem., Int. Ed.*, 2009, **48**, 8512–8515.
- 11 S. Chen, Z. Chen, S. Siahrostami, T. R. Kim, D. Nordlund, D. Sokaras, S. Nowak, J. W. To, D. Higgins, R. Sinclair and J. K. Nørskov, *ACS Sustain. Chem. Eng.*, 2018, **6**, 311–317.
- 12 S. Zhao, X. Zhao, S. Ouyang and Y. Zhu, *Catal. Sci. Technol.*, 2018, **8**, 1686–1695.
- 13 L. Chen, C. Chen, Z. Yang, S. Li, C. Chu and B. Chen, *Adv. Funct. Mater.*, 2021, **31**, 2105731.
- 14 A. Nadar, S. S. Gupta, Y. Kar, S. Shetty, A. P. van Bavel and D. Khushalani, *J. Phys. Chem. C*, 2020, **124**, 4152–4161.
- 15 H. Hirakawa, S. Shiota, Y. Shiraishi, H. Sakamoto, S. Ichikawa and T. Hirai, *ACS Catal.*, 2016, **6**, 4976–4982.
- 16 X. Chen, S. Xiao, H. Wang, W. Wang, Y. Cai, G. Li, M. Qiao, J. Zhu, H. Li, D. Zhang and Y. Lu, *Angew. Chem., Int. Ed.*, 2020, **59**, 17182–17186.
- 17 Z. Lian, F. Wu, J. Zi, G. Li, W. Wang and H. Li, *J. Am. Chem. Soc.*, 2023, **145**, 15482–15487.
- 18 D. Zhang, X. Liu, S. Wang, B. Fan, Z. Shao, C. Su and X. Pu, *J. Alloys Compd.*, 2021, **869**, 159390.
- 19 D. Gao, P. Deng, J. Zhang, L. Zhang, X. Wang, H. Yu and J. Yu, *Angew. Chem., Int. Ed.*, 2023, 202304559.
- 20 A. Kumar, V. Navakoteswara Rao, A. Kumar, A. Mushtaq, L. Sharma, A. Halder, S. K. Pal, M. V. Shankar and V. Krishnan, *ACS Appl. Energy Mater.*, 2020, **3**, 12134–12147.
- 21 A. Kumar, M. Kumar, V. N. Rao, M. V. Shankar, S. Bhattacharya and V. Krishnan, *J. Mater. Chem. A*, 2021, **9**, 17006–17018.
- 22 L. Acharya, S. P. Pattnaik, A. Behera, R. Acharya and K. Parida, *Inorg. Chem.*, 2021, **60**, 5021–5033.
- 23 K. Xiao, T. H. Tsang, D. Sun, J. Liang, H. Zhao, Z. Jiang, B. Wang, J. C. Yu and P. K. Wong, *Adv. Energy Mater.*, 2021, **11**, 2100291.
- 24 B. P. Mishra, L. Biswal, S. Das, L. Acharya and K. Parida, *Langmuir*, 2023, **39**, 957–971.
- 25 S. P. Tripathy, S. Subudhi, S. Das, M. K. Ghosh, M. Das, R. Acharya, R. Acharya and K. Parida, *J. Colloid Interface Sci.*, 2022, **606**, 353–366.
- 26 S. Das, G. Swain and K. Parida, *Sustainable Energy Fuels*, 2022, **6**, 937–953.
- 27 G. Swain, S. Sultana and K. Parida, *Nanoscale*, 2021, **13**, 9908–9944.
- 28 S. Das, G. Swain and K. Parida, *Mater. Chem. Front.*, 2021, **5**, 2143–2172.
- 29 J. Zhang, Y. Wang, J. Cui, J. Wu, Y. Li, T. Zhu, H. Kang, J. Yang, J. Sun, Y. Qin and Y. Zhang, *J. Phys. Chem. Lett.*, 2019, **10**, 3282–3289.
- 30 S. Das, G. Swain, B. P. Mishra and K. Parida, *New J. Chem.*, 2022, **46**, 14922–14932.
- 31 S. Jayabal, G. Saranya, J. Wu, Y. Liu, D. Geng and X. Meng, *J. Mater. Chem. A*, 2017, **5**, 24540–24563.
- 32 S. Das, L. Acharya, L. Biswal, B. P. Mishra and K. Parida, *Catal. Sci. Technol.*, 2023, **13**, 2827–2840.
- 33 C. Zhu, Q. Xian, Q. He, C. Chen, W. Zou, C. Sun, S. Wang and X. Duan, *ACS Appl. Mater. Interfaces*, 2021, **13**, 35818–35827.
- 34 Y. Guo, Y. Ao, P. Wang and C. Wang, *Appl. Catal., B*, 2019, **254**, 479–490.
- 35 G. Swain, S. Sultana and K. Parida, *ACS Sustain. Chem. Eng.*, 2020, **8**, 4848–4862.
- 36 D. Zeng, Z. Lu, X. Gao, B. Wu and W. J. Ong, *Catal. Sci. Technol.*, 2019, **9**, 4010–4016.
- 37 Y. Yang, Q. Wang, X. Zhang, X. Deng, Y. Guan, M. Wu, L. Liu, J. Wu, T. Yao and Y. Yin, *J. Mater. Chem. A*, 2023, **11**, 1991–2001.
- 38 X. Wang, T. Zhu, S. Chang, Y. Lu, W. Mi and W. Wang, *ACS Appl. Mater. Interfaces*, 2020, **12**, 11252–11264.
- 39 H. Xu, J. Yi, X. She, Q. Liu, L. Song, S. Chen, Y. Yang, Y. Song, R. Vajtai, J. Lou and H. Li, *Appl. Catal., B*, 2018, **220**, 379–385.
- 40 L. Acharya, S. Nayak, S. P. Pattnaik, R. Acharya and K. Parida, *J. Colloid Interface Sci.*, 2020, **566**, 211–223.





- 41 S. P. Tripathy, S. Subudhi, A. Ray, P. Behera, G. Swain, M. Chakraborty and K. Parida, *Langmuir*, 2023, 7294–7306.
- 42 H. Cao, Z. Bai, Y. Li, Z. Xiao, X. Zhang and G. Li, *ACS Sustain. Chem. Eng.*, 2020, 8, 7343–7352.
- 43 L. Biswal, L. Acharya, B. P. Mishra, S. Das, G. Swain and K. Parida, *ACS Appl. Energy Mater.*, 2023, 6, 2081–2096.
- 44 X. Wang, T. Zhu, S. Chang, Y. Lu, W. Mi and W. Wang, *ACS Appl. Mater. Interfaces*, 2020, 12, 11252–11264.
- 45 L. Acharya, G. Swain, B. P. Mishra, R. Acharya and K. Parida, *ACS Appl. Energy Mater.*, 2022, 5, 2838–2852.
- 46 L. Jing, Y. Xu, M. Xie, J. Liu, J. Deng, L. Huang, H. Xu and H. Li, *J. Chem. Eng.*, 2019, 360, 1601–1612.
- 47 H. Zeng, Z. Li, G. Li, X. Cui, M. Jin, T. Xie, L. Liu, M. Jiang, X. Zhong, Y. Zhang and H. Zhang, *Adv. Energy Mater.*, 2022, 12, 2102765.
- 48 L. Acharya, B. P. Mishra, S. P. Pattnaik, R. Acharya and K. Parida, *New J. Chem.*, 2022, 46, 3493–3503.
- 49 G. Swain, S. Sultana and K. Parida, *Inorg. Chem.*, 2019, 58, 9941–9955.
- 50 L. Ding, F. Qi, Y. Li, J. Lin, Y. Su, Y. Song, L. Wang, H. Sun and C. Tong, *J. Colloid Interface Sci.*, 2022, 614, 92–101.
- 51 C. Wu, W. Huang, H. Liu, K. Lv and Q. Li, *Appl. Catal., B*, 2023, 330, 122653.
- 52 B. Zhao, X. Wang, P. Liu, Y. Zhao, Y. L. Men and Y. X. Pan, *Ind. Eng. Chem. Res.*, 2022, 61, 6845–6858.
- 53 Z. Lv, P. Liu, Y. Zhao, C. Peng, X. Y. Meng and Y. X. Pan, *Chem. Eng. Sci.*, 2022, 255, 117658.
- 54 Y. Yang, H. Yu, M. Wu, T. Zhao, Y. Guan, D. Yang, Y. Zhu, Y. Zhang, S. Ma, J. Wu and L. Liu, *Appl. Catal., B*, 2023, 325, 122307.
- 55 S. Subudhi, G. Swain, S. P. Tripathy and K. Parida, *Inorg. Chem.*, 2020, 59, 9824–9837.
- 56 G. Swain, S. Sultana, J. Moma and K. Parida, *Inorg. Chem.*, 2018, 57, 10059–10071.
- 57 D. Zhang, R. Zhang, X. Jiang, D. Zhang, H. Li, J. Liu, X. Pu and P. Cai, *Dalton Trans.*, 2023, 52, 14956–14966.
- 58 Y. Xu, J. Ouyang, L. Zhang, H. Long, Y. Song and Y. Cui, *Chem. Phys. Lett.*, 2023, 814, 140331.

